



**HAL**  
open science

# High-Throughput Ammonia Production from Nitrate Using Liquid Metal Synthesized Bismuth Nano-Catalyst

Sahar Nazari, Jing Sun, Mahroo Baharfar, Philippe Poulin, Kourosch Kalantar-Zadeh, Ali Rouhollah Jalili, Dorna Esrafilzadeh

► **To cite this version:**

Sahar Nazari, Jing Sun, Mahroo Baharfar, Philippe Poulin, Kourosch Kalantar-Zadeh, et al.. High-Throughput Ammonia Production from Nitrate Using Liquid Metal Synthesized Bismuth Nano-Catalyst. *Advanced Energy Materials*, In press, 10.1002/aenm.202304287 . hal-04537031

**HAL Id: hal-04537031**

**<https://hal.science/hal-04537031v1>**

Submitted on 8 Apr 2024

**HAL** is a multi-disciplinary open access archive for the deposit and dissemination of scientific research documents, whether they are published or not. The documents may come from teaching and research institutions in France or abroad, or from public or private research centers.

L'archive ouverte pluridisciplinaire **HAL**, est destinée au dépôt et à la diffusion de documents scientifiques de niveau recherche, publiés ou non, émanant des établissements d'enseignement et de recherche français ou étrangers, des laboratoires publics ou privés.



Distributed under a Creative Commons Attribution - NonCommercial - NoDerivatives 4.0 International License

# High-Throughput Ammonia Production from Nitrate Using Liquid Metal Synthesized Bismuth Nano-Catalyst

Sahar Nazari, Jing Sun, Mahroo Baharfar, Philippe Poulin, Kourosh Kalantar-Zadeh,\*  
Ali (Rouhollah) Jalili,\* and Dorna Esrafilzadeh\*

The implementation of renewable energy sources to electrify ammonia (NH<sub>3</sub>) production is identified as a critical approach for achieving successful decarbonization in the pursuit of a more sustainable future. A liquid metal-based method is presented for synthesizing bismuth (Bi) nano-electrocatalysts, enabling efficient and sustainable ammonia production via nitrate electroreduction. Bi-metal precipitated from a gallium liquid metal alloy yields solution-processable Bi and oxide with controllable nanostructures such as nanosheets, nanotubes, and nanoparticles. Combining Bi nano-electrocatalysts and graphene liquid crystals creates self-assembling layered electrocatalytic systems. Integrating 3D printing technology allows for precise control over the geometry, microporosity, and number of deposited layers of the electrocatalytic scaffold electrode, resulting in improved mass transport properties, durability, and the prevention of catalyst detachment. Consequently, the ammonia production rate reaches 400 nmol s<sup>-1</sup> cm<sup>-2</sup>, with a Faradaic efficiency of over 90% and current densities exceeding 350 mA cm<sup>-2</sup>. These numbers indicate the excellent scalability potential of the proposed electrocatalytic system.

## 1. Introduction

Liquid metals are liquid alloys composed of post-transition and zinc group elements that remain in a liquid state at or near room temperature. Gallium (Ga) is widely used and researched among post-transition metals due to its low toxicity and melting point of 29.8 °C.<sup>[1]</sup> Liquid Ga has distinct fluidic and metallic properties that allow it to alloy with a wide range of other post-transition metals.<sup>[2]</sup> By carefully designing Ga-based alloys, preserving fluidity near room temperature is possible. This creates a favorable environment for accommodating metal nanoclusters within the liquid metal alloy.<sup>[3]</sup> Researchers have so far controlled the growth of solute metal structures with a preference for symmetry or orientation during their crystal growth after nucleation by taking advantage of the

structuring and atomic self-arrangement within liquid Ga.<sup>[4,5]</sup> As a result, various crystal morphologies and nanocrystal formation dynamics have been observed in liquid Ga alloy systems.<sup>[6]</sup> To date, utilizing liquid metal alloys, researchers have successfully synthesized nanomaterials through methods such as mechanical agitation, filtration, and a variety of bottom-up strategies.<sup>[7]</sup> However in general, it is challenging to passively separate metallic nanoclusters from the core of the liquid metal alloys due to their high surface tension and surface oxidation.<sup>[8]</sup> In contrast, when segregation occurs via the application of an external electric field while the alloy is still liquid, it is possible to directly and completely expel nanoscale solute metals from the alloy, a process known as “metal expulsion.”<sup>[9]</sup>


Our recent research has demonstrated that electrochemistry can induce direct metal expulsion from liquid alloys using interfacial perturbations.<sup>[10]</sup> When liquid alloys are submerged in electrolytes, a liquid–liquid interface with distinct physical and chemical characteristics is formed. The surface tension of the liquid alloy is altered when an electric current is applied to such an interface. This may result in surface segregation between the liquid alloy and its constituent metals. It has been particularly shown that the discharge of minority elements from a liquid alloy, when a polarizing voltage is applied. Using the alloys GaSn, GaIn, GaZn, and GaBi,<sup>[3,10]</sup> the technique has produced metallic nanostructures with potential applications in multiple energy-related fields, including electrocatalysis.

S. Nazari, J. Sun, M. Baharfar, A. (Rouhollah) Jalili  
School of Chemical Engineering  
University of New South Wales (UNSW) Sydney  
Sydney, NSW 2052, Australia  
E-mail: [ali.jalili@unsw.edu.au](mailto:ali.jalili@unsw.edu.au)

P. Poulin  
Centre de Recherche Paul Pascal–CNRS  
University of Bordeaux  
Pessac 33600, France

K. Kalantar-Zadeh  
School of Chemical and Biomolecular Engineering  
The University of Sydney  
Sydney, NSW 2006, Australia  
E-mail: [kourosh.kalantarzadeh@sydney.edu.au](mailto:kourosh.kalantarzadeh@sydney.edu.au)

D. Esrafilzadeh  
School of Biomedical Engineering  
University of New South Wales (UNSW)  
Sydney, NSW 2052, Australia  
E-mail: [d.esrafilzadeh@unsw.edu.au](mailto:d.esrafilzadeh@unsw.edu.au)

 The ORCID identification number(s) for the author(s) of this article can be found under <https://doi.org/10.1002/aenm.202304287>

© 2024 The Authors. Advanced Energy Materials published by Wiley-VCH GmbH. This is an open access article under the terms of the [Creative Commons Attribution-NonCommercial-NoDerivs License](#), which permits use and distribution in any medium, provided the original work is properly cited, the use is non-commercial and no modifications or adaptations are made.

DOI: 10.1002/aenm.202304287

Among the metals that can be alloyed with Ga for nano-electrocatalyst synthesis, Bi is specifically exciting as it holds significant potential for the electrochemical production of green ammonia.<sup>[11]</sup> Ammonia, the second most produced chemical, is a versatile and foundational compound for synthesizing chemicals and fertilizers. Today, global ammonia demand exceeds 150 million tons annually, consuming over 2% of the world's energy and releasing over 1% of global carbon dioxide emissions.<sup>[12]</sup> Electrocatalytic methods have emerged as a clean energy route for ammonia production at ambient conditions via renewable energy and various infrastructure scales.<sup>[13]</sup> This path is reinforced because ammonia is widely regarded as a potential future zero-carbon fuel source and green hydrogen carrier.<sup>[14]</sup> Although the traditional ammonia production route is highly likely to persist, electrochemical synthesis could substantially contribute to decarbonizing ammonia production, given the vast global demand.

To this end, interest in the electrochemical nitrogen reduction reaction (NRR) for generating ammonia under ambient conditions has increased markedly in recent years.<sup>[15]</sup> This interest is with a focus on improving two key NRR performance metrics: i) ammonia formation selectivity (also known as Faradaic efficiency), and ii) yield rate.<sup>[16]</sup> However, efficient NRR has proven extremely challenging to achieve in practice, given the high triple bond stability of N<sub>2</sub> and its low solubility in water.<sup>[17]</sup> This can shift the N<sub>2</sub> reduction potential into the region where the hydrogen evolution reaction (HER) dominates, leading to low rate and selectivity. Conversely, the electrochemical nitrate (NO<sub>3</sub><sup>-</sup>) reduction reaction does not require the dissociation of high-energy N<sub>2</sub> bonds and thus achieves enhanced reaction rates for NH<sub>3</sub> production.<sup>[18]</sup>

Nitrates, abundantly present in industrial wastewater and polluted groundwater, serve as rich nitrogen sources that can be repurposed for green ammonia synthesis. Additionally, our recent study has presented an energy-efficient and sustainable pathway for nitrate production from air, leveraging renewable energy and a non-thermal plasma process.<sup>[19]</sup> These show that the nitrate reduction pathway can make ammonia and stress the need for efficient and selective electrocatalytic systems, whether from non-thermal plasma or wastewater. To this end, various metals have been proposed as electrocatalysts for nitrate reduction, including noble metals (Ru, Pt, Ir, Ag, and Pd), non-noble metals (Cu, Ni, Fe, Bi, and Co) and their alloys or oxides, as well as single-atom catalysts.<sup>[12]</sup> However, achieving sufficiently active, selective, and stable electrocatalysts remains challenging. Although noble metallic electrodes have demonstrated excellent performance, their high price restricts their widespread application. The development of non-noble metal and nanostructured catalysts with desirable activity, such as Cu nanostructures,<sup>[20]</sup> has demonstrated promise, particularly in acidic environments where they show high rates and Faradaic efficiencies. However, the low durability of Cu catalysts is a significant disadvantage of this metal as a catalyst. For large-scale ammonia production, there is thus a need for the development of practical, durable, and simple to produce electrocatalysts.

Bi-based catalysts, by providing a variety of advantages, may facilitate the electrocatalytic synthesis of ammonia. Bi has a relatively positive standard reduction potential (Bi<sup>3+</sup>/Bi, 0.308 V vs SHE), which makes it an excellent candidate for electrocatalysis. Moreover, Bi-based catalysts have poor HER performance and a

high hydrogen overpotential, allowing them to suppress HER effectively. Due to its relatively low cost and non-toxicity, Bi is also an attractive option.<sup>[11]</sup> In addition, Bi<sub>2</sub>O<sub>3</sub>, a semiconductor with exceptional catalytic, electrical, and optical properties, has a narrow band gap,<sup>[21]</sup> and has proven highly effective for other electrochemical reactions, including NRR,<sup>[11]</sup> and CO<sub>2</sub> reduction.<sup>[22]</sup> Due to its ability to inhibit HER and its high free energy barrier for hydrogen adsorption on its surface, it can achieve high selectivity and Faradaic efficiency when used for nitrate reduction.<sup>[23]</sup>

By manipulating the chemical and nanostructure of Bi catalysts and establishing methods for large-scale solution processing, it may be possible to develop a catalytic system for ammonia production that is highly productive. Numerous chemical approaches have been developed to produce nanomaterials of metallic Bi and its oxides, including metal-organic precursor routes,<sup>[24]</sup> photochemical,<sup>[25]</sup> solvothermal,<sup>[26]</sup> reduction,<sup>[27]</sup> laser ablation methods,<sup>[28]</sup> microwave,<sup>[29]</sup> and liquid-phase exfoliation.<sup>[30]</sup> However, these methods have limitations such as the need for rigorous experimental procedures, high temperatures, toxic organometallic precursors, lengthy reaction times, uncontrollable lateral size and thickness, and unwanted oxidation. Developing nanostructured catalysts that can be readily achieved at a high production rate and a facile process is essential to overcome these challenges. This facilitates subsequent electrode fabrication and enables the utilization of standard and scalable solution processing techniques like casting and 3D printing.

In this study, we develop a metal expulsion method from Ga-Bi liquid metal alloy to produce high-quality and solution-processable Bi nano-electrocatalysts. This procedure induces multiple interfacial processes that facilitate the expulsion of the solute metal, resulting in the precipitation of pure Bi-metal clusters with tunable nanostructure and chemical properties. Combining these Bi nano-electrocatalysts with graphene liquid crystals and 3D printing technology for electrode fabrication resulted in layered and microporous catalytic scaffold electrodes, significantly enhancing the ammonia production rate. This approach offers an excellent solution for creating high-quality Bi nano-electrocatalysts for ammonia synthesis and flexibility for large-scale electrode fabrication, ensuring efficient and industrially acceptable electrocatalytic systems.

## 2. Results and Discussion

### 2.1. Nanoparticles Synthesis

The use of Ga-based alloys offers a unique opportunity to fabricate the production of nanomaterials with adjustable physical and chemical properties.<sup>[10]</sup> While recent studies have focused on synthesizing Bi-based nanomaterials for electrocatalysis,<sup>[11]</sup> the scalable and high-yield synthesis of Bi nano-electrocatalysts using low-melting-point alloys is yet to be explored. Introducing an excess of Bi into liquid Ga metals can create a peculiar dynamic equilibrium, resulting in intriguing phenomena such as nucleation and local ordering of Bi elements.<sup>[9]</sup>

Following the Bi-Ga phase diagram, our primary strategy involves alloying Bi and Ga at 350 °C (Bi: 2.5% and Ga: 97.5% weight percentage).<sup>[31]</sup> Accordingly, Bi at the chosen concentration is a dissolved element in liquid Ga, forming a homogeneous alloy at 350 °C. By controlling the cooling rate of the obtained

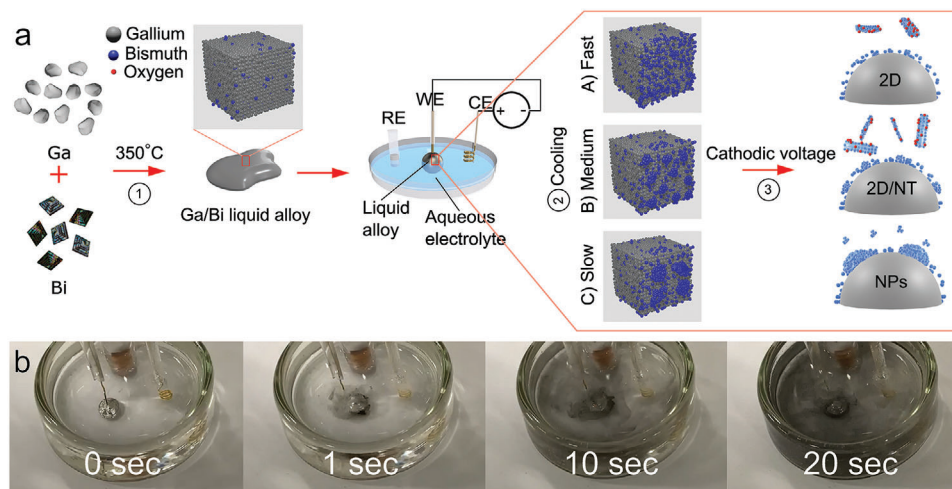


**Figure 1.** a) Schematic illustration of liquid metal alloy preparation and Bi-metal expulsion through electrochemistry. A–C), Cooling from 350 to 80 °C at different rates of 10 (A), 8 (B), and 4 °C min<sup>-1</sup> (C) that resulted in the formation of 2D nanosheets, a mixture of the 2D sheets and NTs, and NPs, respectively. WE is the working electrode, CE is the counter electrode, and SCE is the saturated calomel reference electrode. b) Snapshot of the Bi nanomaterial being expelled into an aqueous solution using cathodic current as a function of time. The electrolyte temperature was maintained at 80 °C, enabling expulsion to occur slightly higher than the alloy's solidification temperature.

alloy near the solidification point at 80 °C, we aim to achieve controlled nucleation and local rearrangement of Bi atoms in the liquid alloy. This process can provide crucial insights into various practical aspects of solidification practice, including morphological development, phase selection, and grain refinement. Subsequently, through electrochemical-assisted metal expulsion, we synthesize nanoparticles for energy applications.

The atoms of Ga and Bi undergo rearrangement in the eutectic binary liquid as it is gradually cooled to a temperature close to solidification. The cooled Ga–Bi alloy, maintained at 80 °C, is submerged in an aqueous electrolyte, establishing a distinct boundary between the two liquids. This boundary enables the extraction of Bi nanoclusters from the alloy, facilitating their expulsion into the aqueous solution, resulting in nanomaterials with diverse morphologies, as illustrated schematically in **Figure 1** (also refer to Video S1, Supporting Information).

Our observations indicate that the rate at which the alloy cools, from 350 to 80 °C, substantially impacts the nucleation and spatial arrangement of bismuth atoms. This led to the formation of various morphologies of migrated Bi atoms on the alloy's surface. Subsequently, these atoms entered the solution and separated from the liquid alloy through the application of the voltage. **Figure 2** shows how applying these two procedures affected the structure and morphology of expelled Bi nanomaterials. A rapid cooling rate of 10 °C min<sup>-1</sup> resulted in the formation of 2D nanosheets in small clusters of  $\gamma$ -/ $\beta$ -Bi<sub>2</sub>O<sub>3</sub> on the alloy surface, as determined by scanning electron microscopy (SEM) analysis (**Figure 2a**). It was also evident that the Bi nanosheets continued to grow by incorporating nanoparticles at their edges, resulting in the expansion of the sheets perpendicular to the alloy surface. In the second set of experiments, we employed a slower cooling process of 8 °C min<sup>-1</sup>, which resulted in the formation of a mixture of thin 2D nanosheets and wrinkled tube-shaped  $\gamma$ -/ $\alpha$ -Bi<sub>2</sub>O<sub>3</sub> nanostructures derived from larger cluster sizes of solidified Bi dissolved in the Ga–Bi alloy (**Figure 2b**). The SEM analysis in-

dicated that the products primarily consist of nanosheets, which have undergone edge rolling due to surface tension, resulting in the formation of nanotube (NT) shaped structures.

According to the classical nucleation theory, which considers a system undergoes with spherical nuclei and a constant nucleation rate, the steady-state volume nucleation rate  $I_{st}$  can be described by the following equation<sup>[32,33]</sup>

$$I_{st} = I_0 \times \exp\left(-\frac{W^* + \Delta G_D}{k_B T}\right) \quad (1)$$

$$I_0 = 2N_1 \frac{k_B T}{h} \left(\frac{a^2 \sigma}{k_B T}\right)^{1/2} \quad (2)$$

$$W^* = \frac{16}{3} \pi \frac{\sigma^3}{\Delta G_V} \quad (3)$$

where  $I_0$  represents the pre-exponential term consisting of the number of structural units  $N_1$  per unit volume of the melt with a mean size  $a$ ,  $k_B$  represents the Boltzmann constant,  $h$  represents the Planck constant, and  $\sigma$  represents the surface energy of the nucleus/melt interface per unit area. The exponential term includes the thermodynamic barrier for nucleation,  $W^*$ , which represents the work of critical cluster formation, and the kinetic barrier for nucleation,  $\Delta G_D$ , represents the activation energy for transporting a structural unit across the nucleus/melt interface. The thermodynamic driving force for crystallization,  $\Delta G_V$ , represents the difference between the free energies of the metal glass and the crystalline phase per unit volume,<sup>[34]</sup> which can be obtained from Equation (4). In this equation,  $\Delta H_m$  is melting enthalpy per unit volume of the crystal at the melting temperature of  $T_m$  with the assumption of zero for the difference of the

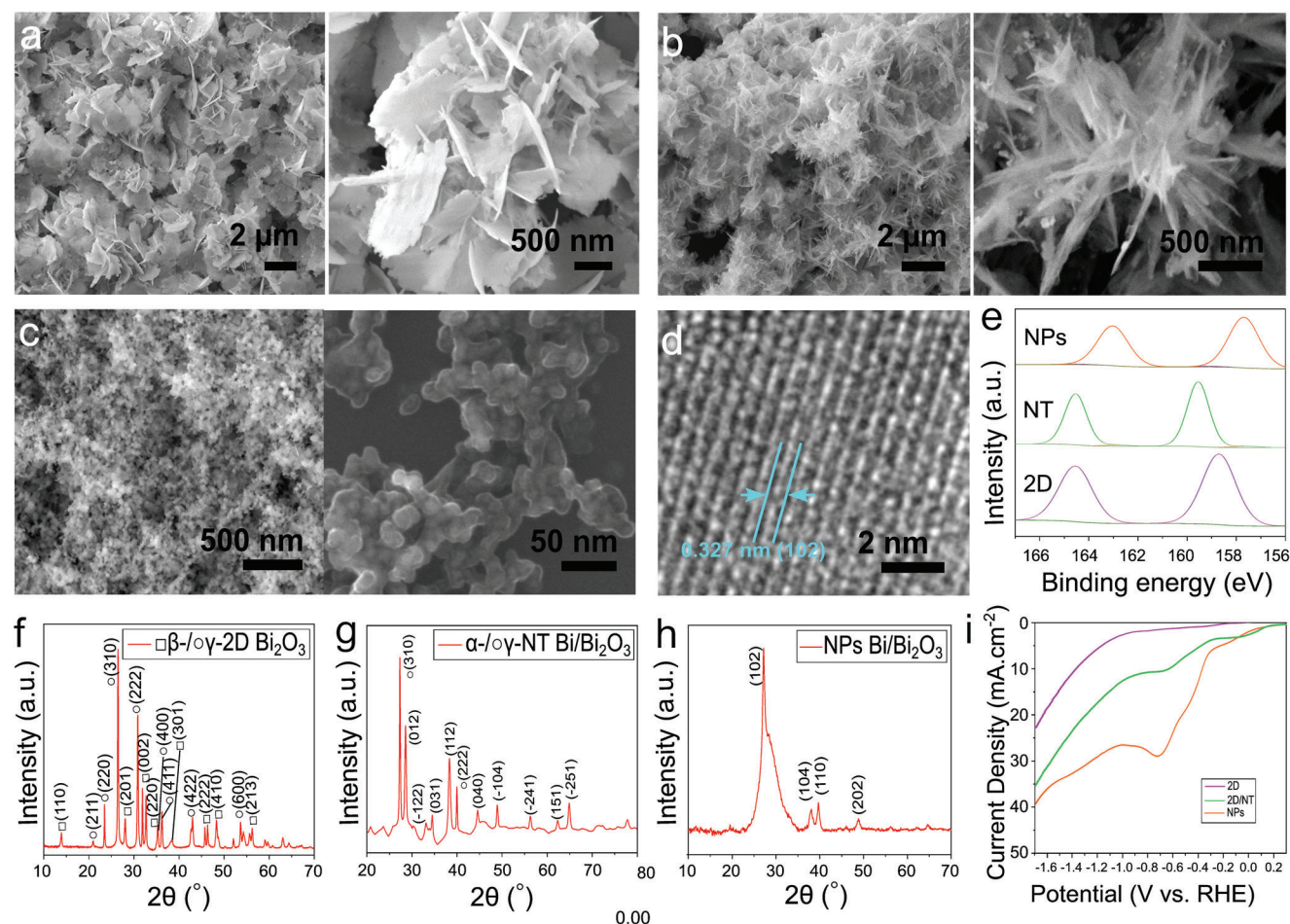


**Figure 2.** Effect of cooling rate on the structure and morphology of expelled Bi nanomaterials. a–c) SEM micrographs of Bi nanomaterials produced at cooling rates of 10 (a), 8 (b), and 4 °C min<sup>-1</sup> (c), respectively. d) High-resolution TEM image featuring the lattice planes (102) Bi<sub>2</sub>O<sub>3</sub>. e) XPS analysis of expelled Bi products. f–h) XRD analysis of expelled Bi nanomaterials produced at cooling rates of 10 (f), 8 (g), and 4 °C min<sup>-1</sup> (h), respectively. i) LSV of nitrate reduction as a function of applied potentials, highlighting the impact of Bi morphology on the electrochemical activity (Electrolyte: 10 mM NaNO<sub>3</sub>+0.5 M Na<sub>2</sub>SO<sub>4</sub> in 10 mM H<sub>2</sub>SO<sub>4</sub>, pH: 1.7).

molar heat capacities of melt and crystal at constant pressure  $\Delta C_p = 0$ .<sup>[35]</sup>

$$\Delta G_V = \frac{\Delta H_m (T_m - T)}{T_m} \quad (4)$$

Different cooling rates significantly impact the nucleation behavior and morphology of Bi atoms that migrated to the surface of the alloy, resulting in the expulsion of various Bi-based nanomaterials. By varying the temperature gradient of the alloy from 350 to 80 °C, we can achieve distinct  $I_{st}$  points. These include nucleation at a consistent rate throughout the entire transformation, saturation of nucleation sites resulting in simultaneous initiation at the transformation's onset, and the occurrence of cellular transformation.<sup>[36]</sup>

The clustering and separation of Bi atoms at the alloy interface depend on the cooling rate. This interdependence can occur due to the size and rate of the nuclei,<sup>[36]</sup> alteration of the surface energy of the liquid alloy and the impact of electrocapillary effects.<sup>[37–39]</sup> The Gibbs adsorption rule describes how the

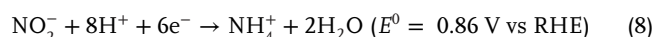
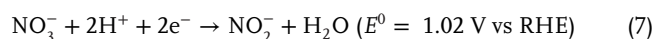
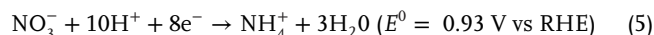
surface energy changes with the composition and temperature of the alloy, and then surface segregation occurs within a thin atomic-scale layer (1–2 atoms thick) at the liquid alloy interface. The manipulation of cooling rates, combined with the impact of electrocapillary effects, allows for an increased depth of perturbation within the liquid alloy. This, in turn, supports the observed variations in the clustering and separation of Bi at the alloy interface. Empirical evidence in the literature indicates that variations in the proportion of components and the speed at which they are cooled can result in different eutectic growth mechanisms and the formation of unique eutectic microstructures.<sup>[40–42]</sup> The solidification of the Ga–Bi eutectic alloy is characterized by a divorced and irregular process. A divorced and irregular process characterizes the solidification of the Ga–Bi eutectic alloy. This is primarily attributed to the low Bi-to-Ga ratio, the liquid state of Ga at the operating temperature, and variations in cooling rate ratios. Higher cooling rates result in smaller cluster sizes and more ordered solidification of dissolved metals, leading to increased strength, hardness, and dislocation density. Conversely, slower cooling rates yield softer, coarser, and less dislocated phases.<sup>[43,44]</sup>

Changes in surface tension and segregation of the liquid alloy are responsible for forming a Bi monolayer or Bi-rich layers at the alloy surface, with a nearly complete Bi monolayer forming under fast cooling and multilayer formation under slow cooling conditions.<sup>[45,46]</sup> When a voltage is applied to the base electrolyte containing the Ga–Bi alloy, electrolysis also occurs, generating positively charged Bi and negatively charged Ga ions. Under the influence of the applied voltage, Bi ions nucleate and grow on the surface of the alloy, forming thin nanosheet Bi nanoparticles. Surface diffusion, driven by the surface energy of the nanoparticles, causes the atoms to rearrange, creating curved tube structures. Simultaneously, larger nanoparticles tend to grow, using the smaller ones as their seeds, through a process known as Ostwald ripening, which further enhances the curvature of the tubes. The structure observed in Figure 2b resembles NTs and is sustained by the cohesive forces of surface tension and surface energy acting on the nanosheets, leading to their rolling motion.

In the third experimental configuration, an even slower cooling rate of 4 °C min<sup>-1</sup> was used, forming a distinct Bi-rich layer on top of the alloy droplet. The subsequent application of a cathodic potential led to the breakdown of the Ga–Bi alloy and the nucleation of Bi atoms on the surface of the alloy. This nucleation process led to the formation of Bi nanoclusters, which expelled Bi nanoparticles (NPs) from the alloy. Figure 2c shows SEM micrographs of NPs clusters at low and high resolution, confirming that the expelled Bi is composed of nanometer-sized particles packed densely, with most NPs ranging in size from 5 to 50 nm. The high-resolution TEM image in Figure 2d shows a d-spacing of 0.327 nm, corresponding to the lattice plane of (102) hexagonal-Bi/Bi<sub>2</sub>O<sub>3</sub>. The formation of small Bi clusters results from the supersaturation of Bi atoms in the surface layer formed during low-temperature cooling. Bismuth atoms diffuse from the bulk of the alloy beneath the surface layer as the clusters expand. The reduction in nanodomain surface energy as clusters grow in size drives the growth process. This sequential procedure culminates in transforming Bi nanodomains into Bi NPs, which involves the coalescence of adjacent clusters and the removal of excess Bi atoms through the top layer.

The metal expulsion process occurred in an aqueous electrolyte, resulting in water splitting and localized acid production, which influenced the chemical properties of the forming Bi nanomaterials. X-ray photoelectron spectroscopy (XPS) analysis (Figure 2e) displayed the spin-orbit components of Bi<sub>4f<sub>7/2</sub></sub> (at 159.1 eV) and Bi<sub>4f<sub>5/2</sub></sub> (164.5 eV), suggesting the presence of bismuth oxide,<sup>[47]</sup> in the 2D and NT nano Bi. On the other hand, XPS analysis of Bi-NPs identifies the presence of two spin-orbit components, Bi<sub>4f<sub>7/2</sub></sub> (157.1 eV) and Bi<sub>4f<sub>5/2</sub></sub> (162.2 eV), which are typical of metallic Bi.<sup>[48]</sup> X-ray diffraction (XRD) analysis of 2D showed a layered structure and high crystallinity of a mixture of tetragonal ( $\beta$ ) and body-centered cubic ( $\gamma$ ) phases (Figure 2f). While the NT exhibits monoclinic ( $\alpha$ ) and body-centered cubic ( $\gamma$ ) crystal phases, as demonstrated by XRD patterns (Figure 2g). However, the XRD pattern of the expelled Bi-NPs revealed that the Bi/Bi<sub>2</sub>O<sub>3</sub> system is a mixture of amorphous and crystalline Bi-NPs, with the predominant amorphous nature of the NPs indicated by the broad hump in the XRD pattern centered at  $2\theta = 28$  (Figure 2h). XRD patterns of amorphous Bi metal frequently display this prominent hump.<sup>[48]</sup>

The formation of Bi nanostructures is affected by nucleation, growth, and transformation processes, resulting in distinct morphological and physical properties that also influence electrochemical performance. Figure 2i illustrates the linear sweep voltammetry (LSV) of the three distinct Bi catalyst morphologies, showing a consistent trend of current density increase as the potential increases to  $-1.7$  versus RHE and a broad redox peak area at  $-0.7$  V versus RHE. The electrochemical conversion of nitrate (NO<sub>3</sub><sup>-</sup>) to ammonia (as NH<sub>4</sub><sup>+</sup>) involves two pathways. The first enables the direct conversion of NO<sub>3</sub><sup>-</sup> to ammonia by exchanging eight electrons at overpotentials lower than the hydrogen generation overpotential (5 and 6), while the second involves a NO<sub>2</sub><sup>-</sup> intermediary step (7 and 8), evident in broad redox peaks centered around  $-0.7$  V versus RHE.<sup>[49]</sup>



This aligns with previous studies indicating a two-step mechanism with NO<sub>2</sub><sup>-</sup> as an intermediate.<sup>[50,51]</sup> The dominant pathway is influenced by the choice of catalyst and electrolyte conditions, with stronger NO<sub>3</sub><sup>-</sup> adsorption favoring direct eight-electron reduction and weaker adsorption promoting the NO<sub>2</sub><sup>-</sup> intermediate pathway. Both pathways can operate concurrently in the electrochemical conversion of NO<sub>3</sub><sup>-</sup> to NH<sub>4</sub><sup>+</sup>, with their relative contribution depending on various factors. Ongoing research aims to optimize catalysts and conditions beyond the scope of this study. The combination of these pathways resulted in a continuous conversion of NO<sub>3</sub><sup>-</sup> to ammonium ions in the electrolyte, leading to a monotonic increase in NH<sub>4</sub><sup>+</sup> concentration at a production rate of  $\approx 16$  nmol s<sup>-1</sup> cm<sup>-2</sup>. Notably, there is a contrast in current density among 2D structures, 2D/NT structures, and NPs in the ammonia synthesis electrolyte. NPs exhibit a significantly higher current density under identical experimental conditions, attributed to their elevated surface area-to-volume ratio and increased conductivity of metallic Bi within the NPs.

Optimizing the physical and electrochemical properties of the Bi electrocatalyst was essential in influencing the overall performance and current density. Nevertheless, it is crucial to recognize that the design, catalyst loading, and production methods all substantially affect the performance of electrodes.<sup>[52]</sup> In our investigation of Bi nanocatalysts, we first focused on achieving a mass loading level suitable for industrial applications (0.1–10 mg cm<sup>-2</sup>), as depicted in Figure 3a,b. Despite efforts to increase the electrochemical current density by increasing the loading of Bi nanoparticles from 0.1 to 3 mg cm<sup>-2</sup>, challenges persisted in attaining industrially acceptable levels of electrocatalytic ammonia synthesis, aligning with the DoE ambitious target of producing 10 kg per day.<sup>[53]</sup> The challenge emerges from the requirement of a current density that surpasses 300 mA cm<sup>-2</sup>, which presents obstacles to achieving the required nitrogen/nitrate reduction to ammonia in industrial settings. However, our findings indicated that increasing the amount of Bi-NPs cast on the electrode

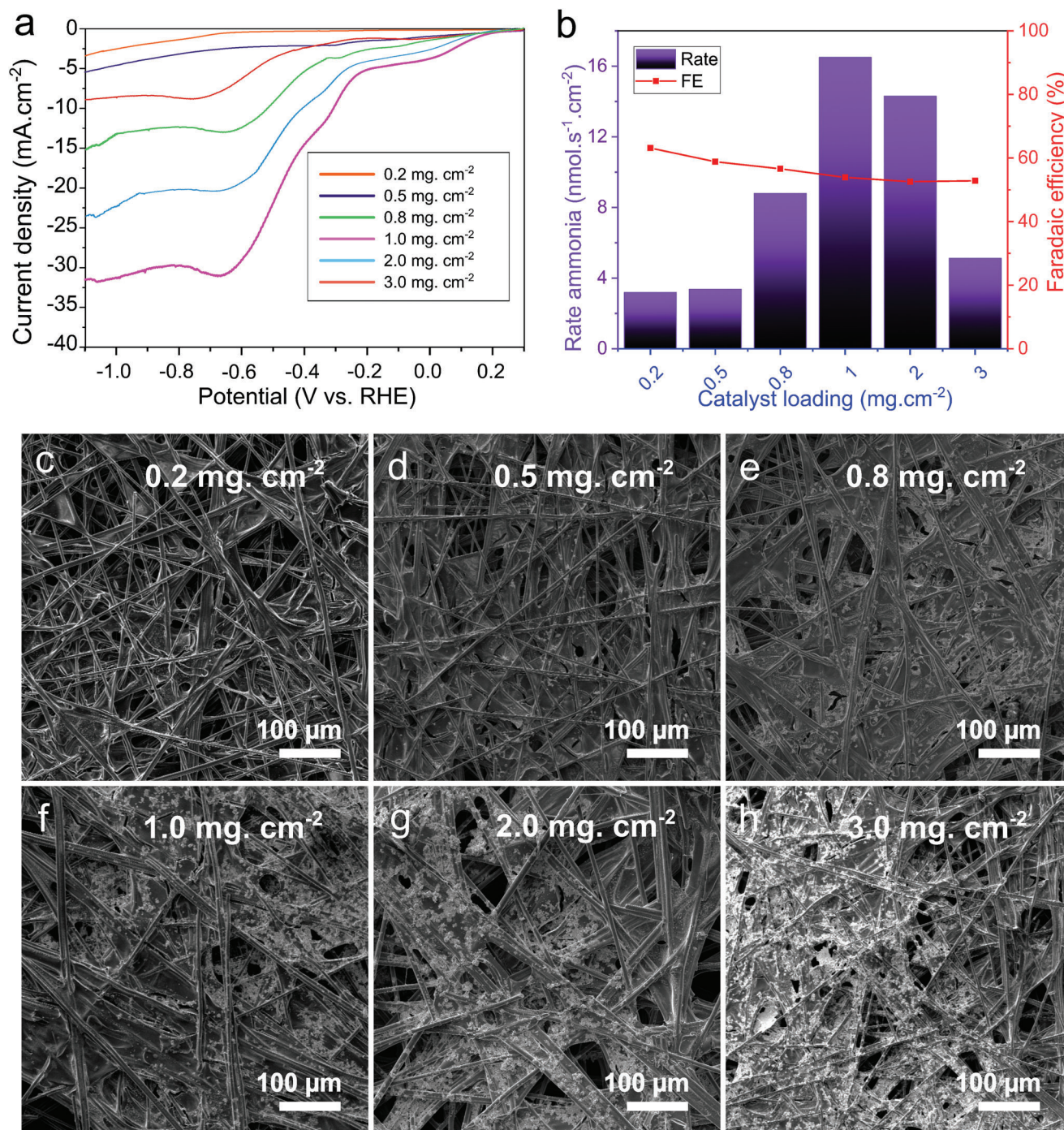


**Figure 3.** The impact of increased mass loading on production rate and current density. a) Linear sweep voltammetry compares the current density of nitrate reduction as a function of catalyst loading (Electrolyte: 10 mM NaNO<sub>3</sub>+0.5 M Na<sub>2</sub>SO<sub>4</sub> in 10 mM H<sub>2</sub>SO<sub>4</sub>, pH: 1.7). b) Compares ammonia production rate and Faradaic efficiency measured of Bi-NPs catalysts as a function of the mass loading. c–h) SEM micrographs of the electrodes produced by casting varying amounts of mass onto the electrode. The mass loadings are indicated in each image.

positively affected performance until loadings reached  $\approx 1$  mg cm<sup>-2</sup>. Beyond this level, higher mass loadings led to the formation of significant clusters of aggregated Bi particles on the surface (Figure 3c–h). Therefore, it was impossible to attain current densities higher than  $\approx 30$  mA cm<sup>-2</sup> for BiNPs catalysts by increasing the mass loading any further than 1 mg cm<sup>-2</sup>.

## 2.2. Composite Synthesis and Catalyst Printing

The electrochemical performance of electrocatalysts is usually evaluated at the lab scale using thin electrodes cast on carbon cloth substrates. Nevertheless, our results demonstrated that achieving commercially viable current densities requires more

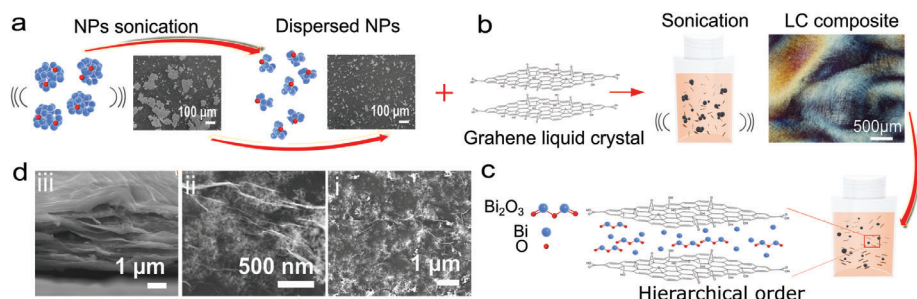


**Figure 4.** Schematic illustration of the procedure used to produce the GO/NPs composite catalyst. a) Demonstrates the method used to achieve a homogeneous dispersion of the expelled NPs in ethanol and the corresponding SEM image of the cast material on a silicon wafer. b) Illustrates the mixing of NPs and GO liquid crystals, followed by ultrasonication of the mixture. The characteristic polarized optical microscopy image reveals that the resulting combination of GO and NPs (ratio 50:50 wt%) forms a liquid crystal phase. c) A schematic illustration of the hierarchical structure of GO/NPs presents the inherent self-assembly properties of the LC, which facilitate the formation of hierarchical structures (conductor–catalyst–conductor). d) SEM images of NPs uniformly dispersed within graphene layers, creating hierarchical structure (i,ii) images obtained by the backscattered electron detector at various magnifications. A cross-sectional view of the hierarchical composite presented at (iii) reveals the GO/Bi NPs catalyst's layer-by-layer assembly.

than simply increasing the mass of catalysts. Furthermore, an additional barrier to the flow of ions and the exchange of electrons is added by the thickness and mass increase of the electrode.

To overcome the challenges of achieving optimal charge delivery and efficient mass transport, we developed a strategy to increase accessible surface area and conductivity while improving catalyst loading. We applied the self-assembly effect of liquid crystals (LC) as mediators to create multilayered and organized structural arrangements, exploiting previous studies highlighting the potential of anisotropic building blocks such as graphene oxide (GO) and their intrinsic self-assembly capabilities.<sup>[54]</sup> We have previously created LC phases that could mimic self-assembly systems by combining nanomaterials and liquid crystals.<sup>[55,56]</sup> Moreover, the reduced GO (rGO) interface can enhance the electrochemical performance of the Bi catalyst by improving electron transfer, surface area, catalyst-electrolyte interaction, stability, and reducing aggregation and agglomeration.

To this end, we developed self-assembled LC composite dispersions by combining Bi NPs and liquid crystals of graphene oxide (LC-GO) (see Figure 4a–c). The Bi NPs were effectively embedded within the well-organized layers of GO, resulting in the formation of layered structures, as observed in the SEM images in Figure 4d. In the backscattered electron images (Figure 4d-i,ii), regions containing heavier elements (i.e., Bi) with higher atomic numbers (*Z* values) appear brighter than GO. This contrast enables clear visualization of Bi-NPs distributed uniformly across the GO surface. The Bi NPs' small size was critical in forming a stable composite suspension with LC-GO and preserving the layered structure during casting. Figure 4d-iii shows cross-sectional SEM images of a typical cast film, which further demonstrates the internal hierarchical structure of the nanocatalyst scaffold constituted of Bi NPs and GO.

To restore electrical conductivity for electrochemical ammonia synthesis, we electrochemically reduced GO to rGO (Figure S2, Supporting Information). Figure 5a illustrates the XRD analysis of Bi and GO before and after the production of the composite, reduction to rGO, and utilization in ammonia synthesis. The spectrum of neat GO is typical with a sharp peak at  $2\theta = 11^\circ$ , corresponding to a layer spacing between graphene sheets of about 8Å. The sharpness of the peak reflects a long-range ordering of

the LC domains. However, the interlayer spacing is too small for the intercalation of individual NPs between atomic monolayers. Nevertheless, the inclusion of NPs strongly affects the LC ordering. Following the process of composite production and reduction, the diffraction peaks exhibit increased width, indicating a shorter-range ordering. The NPs, in fact, introduce defects in the LC structure, which display short-range ordering. This change of structure results from the intimate mixing of small LC-GO domains with NPs at a nanoscale. A complete phase separation at a macro scale would have resulted in no change in the XRD spectra and inefficient electrical coupling. This confirms the effective distribution of Bi-NPs within the GO structure, resulting in a uniformly distributed composite. The XRD pattern did not change after ammonia synthesis, indicating that there was no segregation between rGO and Bi, no change in short-range ordering, and no change in the phase of the Bi catalyst.

To determine the extent of the electrochemical reduction of GO to rGO, the relative amounts of carbon, oxygen, and functional groups in GO were analyzed using XPS (Figure 5b). Four deconvoluted peaks at 284.5, 284.8, 286, and 288–290 eV, which correspond to the C=C and C–C group in aromatic rings, the epoxy-alkoxy (CO) group, and the carboxylate (C=O) group, respectively, were observed in the high-resolution C 1s XPS spectra of the as-prepared GO sample. The intensities of all C 1s peaks related to carbon–oxygen bonds decreased in the spectra of the reduced sample, with the CO peak showing a significant reduction. The peaks centered at 284.5 eV, which are characteristic of C=C bonds, became the most prominent simultaneously. These findings indicate that the electrochemical reduction process effectively removed the majority of oxygen-containing functional groups and transformed SP<sup>3</sup> carbons into conjugated SP<sup>2</sup> bonds, which are characteristic of reduced graphene oxide. Notably, the reducing environment of the ammonia synthesis could further remove the residual C–O and C=O groups, implying that the electrical conductivity of graphene can further increase during the test.

The XPS analysis in Figure 5c shows a slight oxidation of Bi-NPs during composite preparation, likely due to bath sonication and GO interaction. Samples with GO exhibit higher oxidation levels compared to those without GO. The XPS spectra reveal a



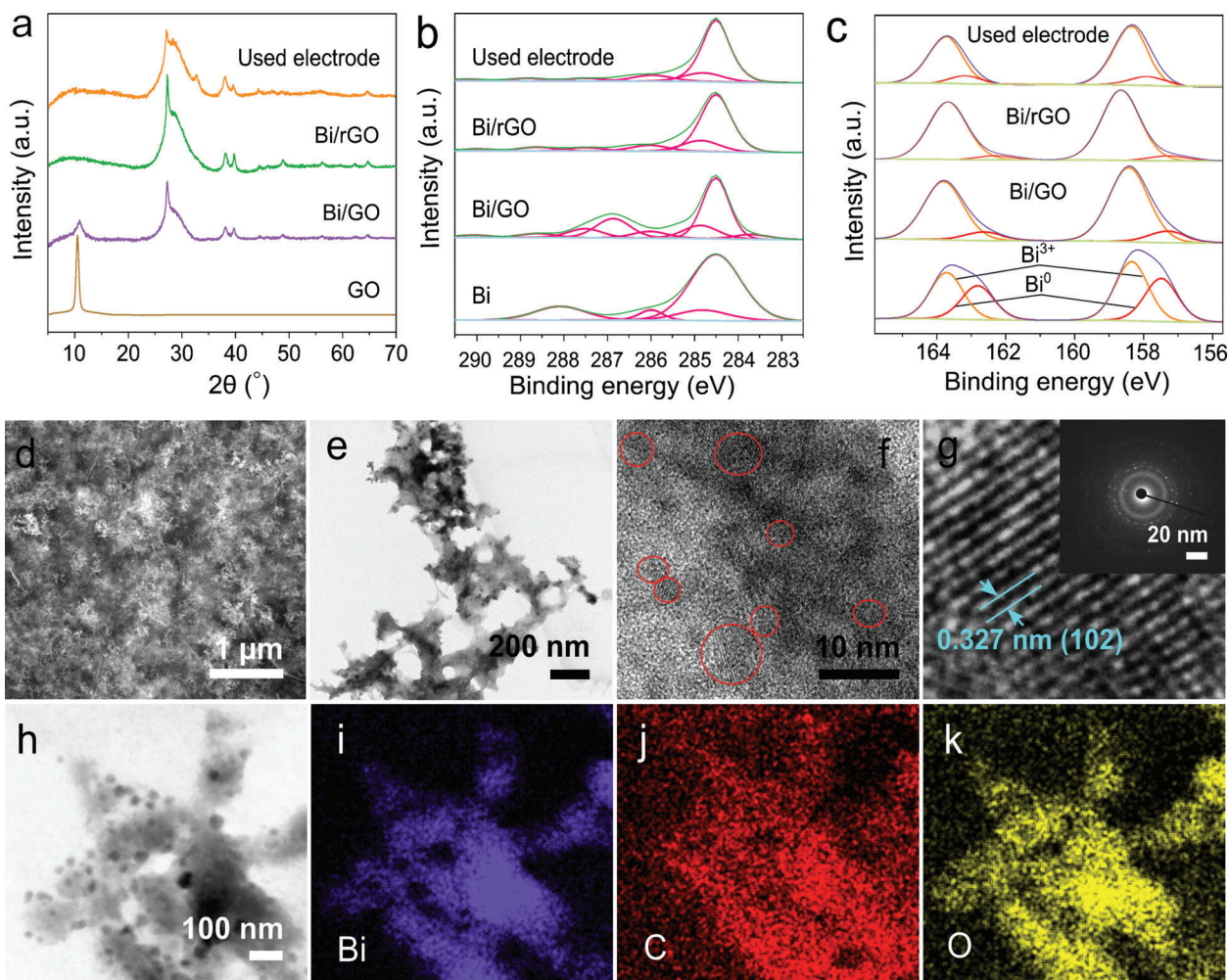


**Figure 5.** Characterization of the GO/Bi NPs composite during and after the electrochemical processes (GO reduction followed by nitrate electroreduction to ammonia). a) XRD patterns and b,c) XPS analysis of the composites before and after the electrochemical processes. d) SEM of the electrode after electroreduction reveals that the catalysts remained embedded within the layers of rGO with no agglomeration or segregation; Bi NPs appear as bright spots within the rGO matrix. e) TEM image exhibits dispersed Bi NPs within the rGO matrix as small dots. f,g) High-resolution TEM images show a mixed structure of crystalline lattice planes (102) Bi/Bi<sub>2</sub>O<sub>3</sub> and amorphous regions. Red circles in (f) denote the crystalline Bi NPs, and the corresponding SAED pattern reveals the primary crystallographic planes of the hexagonal Bi/Bi<sub>2</sub>O<sub>3</sub>. h–k) EDS analysis showing the micro-scale chemical composition of the composite; bismuth (i), carbon (j), and oxygen (k).

decrease in the intensity of Bi<sub>4f<sub>7/2</sub></sub> and Bi<sub>4f<sub>5/2</sub></sub> peaks, along with the appearance of new peaks. The reduction of GO in the composite (Bi/rGO) did not lead to the reversion of Bi-NPs oxidation. Despite this oxidation, the electrochemical performance of the Bi/rGO was not adversely affected (see next section) due to two factors: their proximity to highly conducting graphene and their extremely small size. This effect is consistent with previous reports on bismuth and bismuth oxide-graphene composites used in electrochemical processes, where the advantageous properties of the nanomaterials mitigated the impact of oxidation on their overall performance.<sup>[57]</sup> Also noteworthy is that the Bi NPs in the used electrode showed marginally increased metallic characteristics. This is evident from the increased intensity of the Bi<sub>4f<sub>7/2</sub></sub> (157.1 eV) and Bi<sub>4f<sub>5/2</sub></sub> (162.2 eV) peaks, which indicate more metallic Bi.

The SEM of the electrode after electrochemical reduction shows that the catalysts remained embedded within the lay-

ers of rGO with no aggregation or segregation, as illustrated in Figure 4d. High-resolution TEM analysis shown in Figure 5e–k confirms a combination of crystalline lattice planes (102) Bi/Bi<sub>2</sub>O<sub>3</sub> and amorphous regions, consistent with XRD data. SAED pattern supports the hexagonal Bi/Bi<sub>2</sub>O<sub>3</sub> structure, matching XPS data. Furthermore, it demonstrates that there is no alteration caused by the production of the composite or the subsequent electrochemical process. EDS analysis verifies the incorporation of all Bi-NPs catalysts into the rGO matrix, with Bi, C, and O as the most abundant elements in the composite.

To assess the intrinsic electrochemical activity of the LC-rGO/NPs catalysts synthesized at different LC-rGO/NPs ratios, we performed LSV, as shown in Figure 6a. The obtained polarization curves demonstrate an apparent increase in the collected current densities (*j*) as the LC-rGO ratio increases. This trend continues until the LC-rGO ratio reaches 50 wt% when the current density reaches its maximum value. Notably, the current density

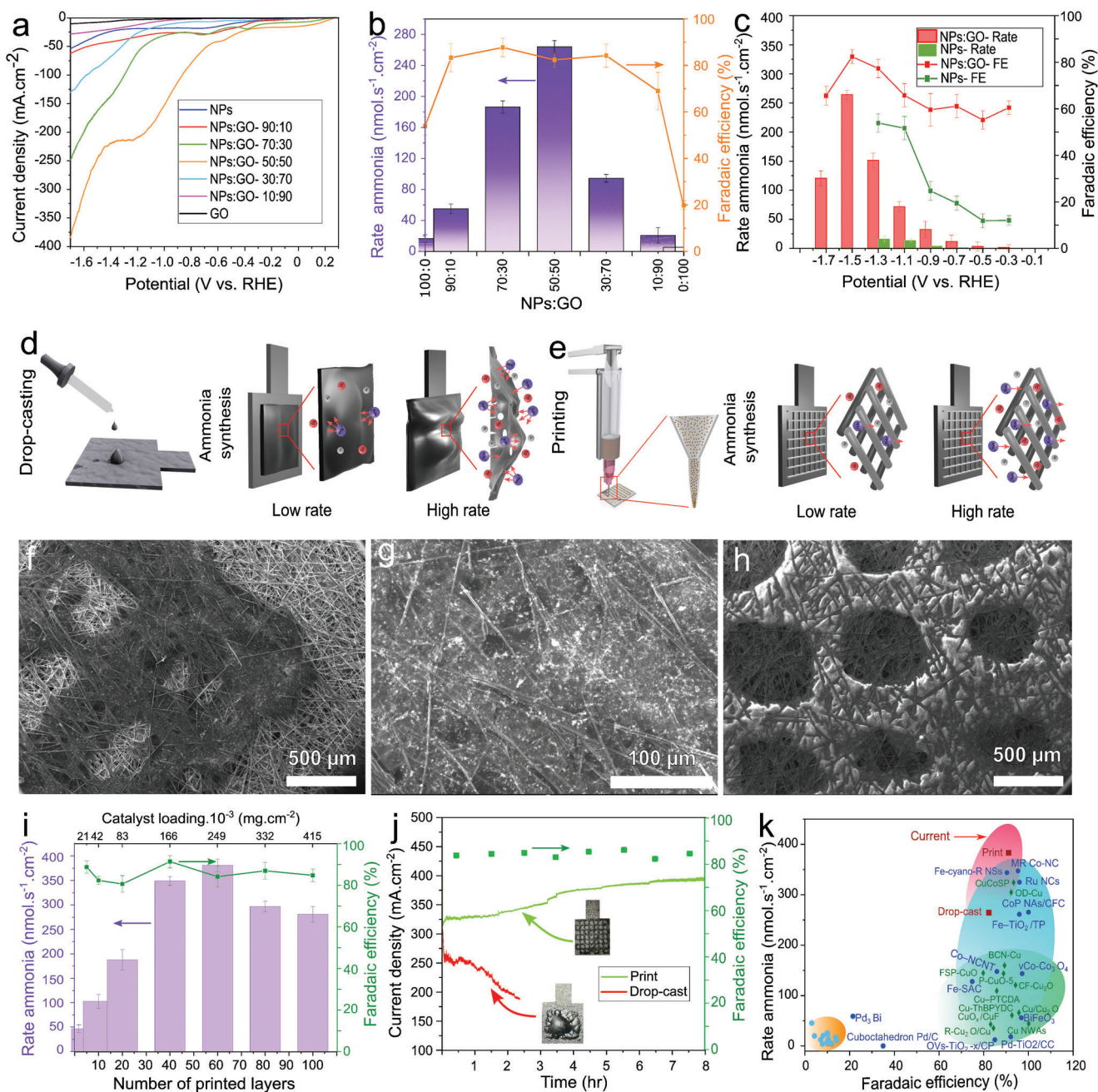


**Figure 6.** Electrochemical reduction of nitrate to ammonia via LC-rGO/NPs catalysts (Electrolyte: 10 mM NaNO<sub>3</sub>+0.5 M Na<sub>2</sub>SO<sub>4</sub> in 10 mM H<sub>2</sub>SO<sub>4</sub>, pH:1.7). a) Linear sweep voltammetry comparing the current density of nitrate reduction as a function of applied potentials, emphasizing the influence of Bi/LC-rGO mass ratio on ammonia synthesis. b) Compares ammonia production rate and Faradaic efficiency measured at -1.5 V versus RHE for LC-rGO/NPs catalysts prepared with various ratios. c) Compares ammonia production rate and Faradaic efficiency of LC-rGO/NPs catalysts (50:50) as a function of applied potential. d,e) Schematic representation of the challenges associated with ion transport at high current densities; cast film (d) and 3D-printed catalysts (e). f,g) SEM micrographs of a typical 3D-printed LC-rGO/NPs catalyst at various magnifications on top of a carbon fiber electrode. A higher image magnification (g) reveals that Bi catalysts are distributed uniformly. h) The back side of the 3D-printed electrode demonstrates that the LC-rGO/NPs catalysts are well-integrated within the support carbon fiber electrode, enhancing durability at high ammonia production rates. i) Comparing the ammonia production rate and Faradaic efficiency of LC-rGO/NPs catalysts as a function of catalyst number and weight in printed layers. j) Prolonged ammonia production tests highlight the increased durability due to the printed microchannels in the scaffold electrodes compared to the cast film. There are also photographs of the used electrodes for comparison. k) Benchmarking the LC-rGO/NPs to other state-of-the-art ammonia production catalysts under comparable conditions. Catalysts are color-coded to facilitate combination and grouping of distinct groups. The brown cycle shows the best-performing nitrogen reduction reaction. Green: Cu-based catalysts, blue: transition and noble metals, and red: Bi-NPs in nitrate reduction (Table S1, Supporting Information).

at  $-1.7$  V versus RHE increases significantly from 50 to 380 mA  $\text{cm}^{-2}$  when the LC-rGO ratio increases from 0 to 50 wt%, respectively. The ammonia production rate (Figure 6b) observed a similar trend, which peaked at  $\approx 260$  nmol  $\text{s}^{-1}$   $\text{cm}^{-1}$  when a 50:50 ratio of LC-rGO/NPs was used. Simultaneously, the Faradaic efficiency toward ammonia ( $\text{FE-NH}_4^+$ ) increased from  $\approx 15\%$  to a maximum of around 90% when at least 30% LC rGO was used as a support matrix and up to parity. This phenomenon can be attributed to various factors, including the optimal interaction between the two components of NPs and rGO at a 50:50 mass ratio. This interaction will facilitate efficient electron transfer and charge transport during the catalytic process. Additionally, the distinctive properties of NPs and rGO, encompassing their respective surface areas, electronic structures, and chemical functionalities, are likely to synergistically contribute to the observed heightened catalytic activity at the 50:50 mass ratio. Moreover, the 50:50 mass ratio offers an optimal surface coverage of rGO on the NPs. This configuration ensures the maximum exposure of catalytically active sites, thereby promoting more active sites for nitrate reduction reactions. Furthermore, the distribution and dispersion of NPs on the rGO sheets and between the layers play a key role in the observed superior overall catalytic efficiency.

Figure 6c compares the performance of NPs electrocatalysts and LC-rGO-supported NPs as a function of electroreduction potential. Compared to Bi-NPs alone, the LC-rGO-supported catalyst exhibits an almost one-order-of-magnitude increase in ammonia production rate and a significantly higher Faradaic efficiency. This improvement highlights the advantages of the layer-by-layer, conductor-catalyst-conductor arrangement of self-assembled LC-rGO/NPs, contributing to enhanced ammonia production and overall catalyst activity. However, the high current density resulting from the increased activity of the catalysts and subsequent excessive ion movement in and out of the electrodes caused instability for both samples. This effect was particularly pronounced in the case of Bi-NPs-only electrodes, as tests at potentials greater than  $-1.3$  V versus RHE were challenging, leading to experiment failure within 15 min. Similarly, the performance of the LC-rGO/NPs film notably declined at potentials higher than  $-1.5$  V versus RHE. This phenomenon is demonstrated schematically in Figure 6d, highlighting the challenges in maintaining the stability and long-term performance of the electrocatalysts under conditions requiring efficient transport of reactants and products within the electrode.

To address the stability issue caused by excessive ion movement within the scaffold electrode, we developed a solution that incorporates 3D-printed microchannels. Our recent research further supports this strategy, highlighting the high potential of 3D printing for fabricating high-performance devices.<sup>[55]</sup> Figure 6e is a schematic representation of the role that 3D printed channels have under conditions of high current density and mass transfer. Figure 6f–h shows SEM micrographs of a typical 3D-printed LC-rGO/NPs catalyst on top of a carbon fiber support electrode at various magnifications. The SEM images show a uniform distribution of Bi electrocatalysts across the printed scaffold electrode and between the graphene layers, in addition to the diffusion of printed catalysts within the support electrode. Furthermore, the backside view of the 3D printed electrode reveals that the LC-rGO/NPs catalysts are well-penetrated and thus integrated within

the support carbon fiber electrode, supporting higher durability even at high ammonia production rates.

Figure 6i shows the impact of controlled catalyst loading through 3D printing on electrocatalytic ammonia production. The electrocatalytic performance steadily improved, reaching its peak at the 60th printed layer with a maximum ammonia production rate of 381 nmol  $\text{s}^{-1}$   $\text{cm}^{-2}$  and a Faradaic efficiency exceeding 90%. Notably, the drop-cast sample, with a loading of 0.5 mg  $\text{cm}^{-2}$ , achieved a lower ammonia production rate of 264 nmol  $\text{s}^{-1}$   $\text{cm}^{-2}$  compared to the 3D-printed electrode with only half the loading (0.246 mg  $\text{cm}^{-2}$ ). The superior performance of 3D-printed LC-rGO/NPs nanostructures can be attributed to the precise control over the scaffold electrode's geometry and thickness, facilitating efficient ion transport. This controlled 3D printing improved ammonia production rates while maintaining high Faradaic efficiency and electrode durability. The significance of microchannels formed during printing is highlighted, enhancing performance and reducing the required catalyst amount by improving ion access to active sites through these channels rather than relying solely on surface diffusion.

We performed extended ammonia production tests to determine the durability of the LC-rGO/NPs electrocatalysts to assess the resilience of the 3D-printed scaffold electrodes. The results of prolonged electroreduction tests comparing cast electrodes to 3D-printed LC-rGO/NPs electrocatalysts with integrated microchannels are shown in Figure 6j. In the cast catalysts, the production rate dropped significantly after 3 h due to the electrode's inability to withstand the high current density and production rate. However, with current densities exceeding 300 mA  $\text{cm}^{-2}$  and FE remaining stable at above 85%, the printed electrodes demonstrated noticeably better durability than the cast electrodes. As described earlier, this could be attributed to the need to transport a significant quantity of reactants, the formation of bubbles, and the transportation of products within the layered electrode. Consequently, the cast film deposited on the carbon fiber electrode gradually deformed and detached from the surface. In contrast, by incorporating microchannels, we achieved more significant control over the catalyst loading, optimizing the current density while improving mass transport and preventing bubble accumulation beneath the layered catalysts. As in this study, this 3D design prevented the catalyst film from detaching from the electrodes, particularly under high current density conditions.

Prolong tests additionally demonstrate that the performance of printed electrodes gradually improves over time, driven by the inherent characteristics of rGO and its response to electrochemical processes. Initially, the presence of residual oxygen-containing functional groups on the fresh rGO surface limits electrolyte penetration, leading to a reduced active surface area and performance constraints. However, during the electrochemical reduction of nitrate to ammonia, the reducing environment acts on the rGO, eliminating some of these surface groups. These results in increased electrical conductivity, improved wettability, and enhanced electrolyte access, ultimately contributing to enhanced device performance. This phenomenon is consistent with findings from previous studies,<sup>[58,59]</sup> in which extended experiments with rGO-based electrochemical devices demonstrated performance enhancement.

When benchmarking the LC-rGO/NPs to other state-of-the-art nitrate reduction electrocatalysts under comparable conditions (Figure 6k and Table S1, Supporting Information), we observe that the LC-rGO/NPs catalysts outperform all others with a higher ammonia yield at Faradaic efficiency over 90%. LC-rGO plays a crucial role in preventing the aggregation of the catalyst particles, ensuring better dispersion and interaction between the NPs and the graphene substrate, and maximizing the electrocatalytic properties of each constituent. This enhanced dispersion makes more active sites accessible, thereby increasing the rate of ammonia production. In addition, graphene's electrical conductivity enables efficient charge distribution across the catalyst surface, minimizing charge accumulation and preventing electrocatalyst deactivation during nitrate reduction. The strategy demonstrated that 3D-printed porous electrocatalytic structures played a crucial role in enhancing mass transport properties by shortening ion and electron pathways while preserving a large active area. This capability is vital as it addresses the limitations of conventional random mixing processes on composite performance and durability.<sup>[60]</sup>

### 3. Conclusions

Using electrochemical methods to produce green ammonia is crucial for realizing net-zero objectives and ensuring sustainable manufacturing. A liquid metal was produced by alloying Bi and Ga at 250 °C. It was then gradually cooled to 80 °C, which is slightly above the solidification temperature of the liquid metal alloy. Subjecting this alloy to a subsequent electrical current enabled the production of Bi nanomaterials that can be dispersed within a liquid media. The morphology of the Bi nanomaterials exhibited flexibility, with adjustments to the cooling rate resulting in the formation of 2D platelets, rolled 2D sheets (nanotubes), or nanoparticles. Among these morphologies, Bi nanoparticles demonstrated superior electrochemical properties for ammonia synthesis through nitrate reduction. Combining Bi nanoparticles with graphene liquid crystals led to the creation of a self-assembled layered scaffold electrode. This self-assembly process regulates the spatial order and Bi distribution between graphene sheets, promoting efficient interaction between ions and Bi nanoparticles. Such scaffold electrode design tackles the issues related to the high loading of electrocatalysts on the electrode while also preventing the aggregation of catalysts. Utilizing 3D printing further improved the performance and durability of our system and supported high-performance, environmentally friendly ammonia synthesis at industrially feasible current densities of >300 mA cm<sup>2</sup>. This development offers a promising approach to sustainably producing ammonia and supports sustainable energy solutions.

### 4. Experimental Section

**Materials for Synthesis of the Catalysts:** Gallium beads, sourced from Indium Corporation (USA), in their 99.999% pure form, and bismuth ingots, obtained from Rotometals (USA), in their 99.999% pure form, were used as received for alloy preparation. Sodium hydroxide (NaOH) pellets and potassium chloride (KCl) powder were obtained from Chem-Supply, Pty., Ltd. Milli-Q water with an electrical resistance of 18.2 MΩ cm at 25 °C was used for all experiments.

**Alloy Preparation for Synthesis of the Catalysts:** To create the gallium–bismuth binary liquid eutectic alloy (Bi: 2.5, Ga: 97.5 weight percentage), a mixture of 48.75 grams of Ga and 1.25 grams of Bi was introduced into a 20 mL glass vial. The vial was then subjected to a temperature of 350 °C on a hotplate, and the metals were allowed to melt for 30 min. The molten metals were carefully stirred using a glass rod to achieve uniform fusion. It is worth noting that based on the diagram phase, the resulting gallium–bismuth alloy possesses a melting point of ≈75 °C.

**Electrochemical Diagnosis for Synthesis of the Catalysts:** Electrochemical analysis of metals was carried out using a CHI650E potentiostat (CH Instruments Inc., USA). For electrochemical measurements, a three-electrode cell configuration was employed with the working electrode consisting of a metal or alloy (0.27 g), a saturated calomel electrode serving as the reference electrode, and a gold counter electrode, unless otherwise specified. A gold wire (0.25 mm diameter) established a connection with liquid metals. The electrochemical cell, a glass Petri dish (35 mm diameter), was filled with 5.5 mL of electrolyte. Before use, the electrolytic solutions were degassed by bubbling nitrogen gas through them for 15 min. All experiments were conducted on a hot plate at a temperature of 80 °C.

**Metal Expulsion for Synthesis of the Catalysts:** A three-electrode cell configuration was employed. The working electrode consisted of a 50 μL sample of the gallium–bismuth liquid alloy, as described in the previous section. A chronoamperometry protocol was used for voltage application, with a sample interval of 0.05 s and sensitivity set at 0.10 A V<sup>-1</sup>. Three different morphologies, namely 2D, a mixture of fine 2D and NTs, and NPs, were generated by cooling the alloy using three different cooling rates. The cooling rates were as follows: directly cooling down from 350 to 80 °C, cooling at a rate of 40 °C per 5 min, and cooling at a rate of 20 °C per 5 min. These cooling processes were conducted in a 0.10 M NaOH and 1.0 M KCl system at -2.70 V and 80 °C, with a gold wire as the counter electrode.

**Reagents and Materials for Synthesis of Ammonia:** All necessary reagents and solvents were procured from Sigma-Aldrich or Chem-Supply Pty Ltd.

**Electrochemical Evaluation for Synthesis of Ammonia:** The electrochemical evaluations were conducted using a CHI650E potentiostat (CH Instruments Inc., USA) in conjunction with a custom H-type electrochemical cell. The cell comprised two chambers separated by a Nafion 117 membrane obtained from the Fuel Cell Store. The working electrode (WE) utilized a 3D-printed scaffold electrode with finely tuned microfluidic properties. A platinum wire served as the counter electrode (CE), while the reference electrode (RE) was an Ag/AgCl electrode in a saturated KCl solution. The background electrolyte consisted of 0.5 M Na<sub>2</sub>SO<sub>4</sub> in 10 mM H<sub>2</sub>SO<sub>4</sub>, with the acid concentration optimized accordingly. The cathodic chamber had a volume of 50 mL, allowing for electrolyte sampling, and the electrode size was 1 cm<sup>2</sup>. Carbon fiber and graphene oxide were employed as control samples, and a magnetic stirrer was set at 500 rpm to facilitate the reaction.

**Ammonia Detection for Synthesis of Ammonia:** A 0.5 mL electrolyte sample from the cathodic chamber was transferred to a 2 mL sample tube. To the tube, 0.4 mL of 1 M NaOH solution (containing 5 wt% salicylic acid and 5 wt% sodium citrate), 0.1 mL of 0.05 M NaClO, and 30 μL of 1 wt% C<sub>5</sub>FeN<sub>6</sub>Na<sub>2</sub>O (sodium nitroferrocyanide) in water was added. The mixture was then incubated in the dark at room temperature for 2 h before UV–vis testing. A calibration curve was prepared using standard solutions of (NH<sub>4</sub>)<sub>2</sub>SO<sub>4</sub> in 10 mM H<sub>2</sub>SO<sub>4</sub> with the indophenol blue reagents mentioned above to determine the concentration of ammonia. The absorbance of the indophenol blue was measured at 655 nm after 2 h. The detection limit for UV–vis analysis was defined as the absorbance at 655 nm, with the lower limit set as the blank 0.5 M Na<sub>2</sub>SO<sub>4</sub> in 10 mM H<sub>2</sub>SO<sub>4</sub> and the upper limit as 200 μM NH<sub>4</sub><sup>+</sup>.

**Faradaic Efficiency and Production Rate Evaluation for Synthesis of Ammonia:** The performance of ammonia synthesis was evaluated based on two key indicators: Faradaic efficiency and ammonia production rate. Faradaic efficiency measures the selectivity of the electrocatalyst for ammonia synthesis. It was determined by the ratio of electrical energy consumed for

ammonia synthesis to the total energy in the electrochemical system. It can be calculated using the following equation

$$\eta = \frac{n \times F \times C \times V}{Q} \quad (9)$$

In the equation,  $n$  represents the number of electrons required for synthesizing one ammonia molecule ( $n = 8$  for nitrate),  $F$  denotes the Faraday constant ( $96\,485.33\text{ C mol}^{-1}$ ),  $C$  signifies the detected ammonia molar concentration,  $V$  represents the volume of the electrolyte, and  $Q$  corresponds to the total electrical energy applied to the electrodes. The number of electrons exchanged was determined by measuring the nitrate concentrations before and after each reaction.

The rate of ammonia production ( $R$ ) was determined by dividing the amount of ammonia produced by the time elapsed and the electrode surface area. The formula for calculating  $R$  is as follows

$$R = \frac{C \times V}{t \times S} \quad (10)$$

where  $t$  signifies the reaction time, and  $S$  corresponds to the surface area of the catalytically active electrode.

**Materials for 3D-Printing:** GO was synthesized using a mixture of natural graphite powder (1 g) and sulfuric acid (200 mL), stirred for an hour.  $\text{KMnO}_4$  (10 g) was then added and stirred for 24 h. The mixture was cooled in an ice bath, and Milli-Q water (200 mL) was added before 50 mL of  $\text{H}_2\text{O}_2$  was stirred for 30 min. The GO particles were washed and centrifuged three times with a 9:1 water/HCl solution and then further washed with Milli-Q water until the pH reached 4–5. Ethanol was prepared from Chem-Supply, Pty., Ltd, and prepared BiNPs catalyst.

**Method for 3D-Printing:** In this study, the material used in the Hyrel 3D printer (Engine High Resolution, USA) mixture of BiNPs, GO, and ethanol. The extrusion rate of the materials was adjusted based on the needle and material concentration. The printing parameters used were as follows: speed: 15–100 mm  $\text{s}^{-1}$ , nozzle: 28 gauge, GO diluted in ethanol (1 mg  $\text{mL}^{-1}$ ):Bi/ $\text{Bi}_2\text{O}_3$  nanostructure (0.82 mg  $\text{mL}^{-1}$ ): 1:1.

**Characterization:** In this study, the morphology and elemental distribution of the samples were characterized using field-emission SEM (Nova Nano SEM) and TEM (JEOL JEM-F200) equipped with an EDS detector and a GATAN ORIUS camera. Direct digital imaging was used for morphological and structural analysis. To prepare the samples for SEM imaging, they were suspended in ethanol, drop-casted onto silicon wafers, attached to double-sided carbon tape, and loaded into the SEM machine. To prepare TEM samples, they were suspended in ethanol, drop-casted onto a lacey carbon grid, left to dry at room temperature, and loaded into the TEM instrument using a double-tilt holder.

High-resolution XPS patterns were collected using the Thermo Scientific ESCALAB250i XPS instrument with a 1486.68 eV Al K $\alpha$  monochromatic soft X-ray source. The scanning parameters were set as follows: background vacuum of  $2 \times 10^{-9}$  mbar, power of 120 W (13.8 kV  $\times$  8.7 mA), 90° photoelectron take-off angle, and 500 mm spot size. The binding energy of 284.8 eV for adventitious hydrocarbon's C 1s peak was used as the reference. To perform XPS depth-profile analysis, samples were suspended in ethanol and dropped onto gold wafers, then allowed to dry at room temperature. Etching was performed using a 1.0 keV Ar ion beam with a reference etching rate of 0.18 nm  $\text{s}^{-1}$ .

The XRD patterns were obtained using an expert Multipurpose X-ray diffraction system (PANalytical, with a wavelength of 1.54 Å and Cu K $\alpha$  radiation) to obtain structural characterization. The parameters for the acquisition were: voltage of 45 kV, current of 40 mA,  $2\theta$  range from 10° to 70°, time pre-step of 120 s, and a step size of 0.026°.

## Supporting Information

Supporting Information is available from the Wiley Online Library or from the author.

## Acknowledgements

The Australian Research Council financially supported this work under the Discovery Early Career Research Award to D.E. (DE230101617) and A.R.J. (DE180100215).

Open access publishing facilitated by University of New South Wales, as part of the Wiley - University of New South Wales agreement via the Council of Australian University Librarians.

## Conflict of Interest

The authors declare no conflict of interest.

## Data Availability Statement

Data is available upon request.

## Keywords

3D printing, electrocatalyst, green ammonia, liquid metal alloy, nitrogen fixation

Received: December 11, 2023

Revised: January 22, 2024

Published online:

- [1] J. Zheng, A. Sharma, T. Kumeria, Y. Chi, M. B. Ghasemian, G. Mao, J. Tang, P. Kumar, M. A. Rahim, K. Kalantar-Zadeh, *Adv. Funct. Mater.* **2023**, *33*, 2300969.
- [2] S. Handschuh-Wang, F. J. Stadler, X. Zhou, *J. Phys. Chem. C* **2021**, *125*, 20113.
- [3] F.-M. Alliou, M. B. Ghasemian, W. Xie, A. P. O'Mullane, T. Daeneke, M. D. Dickey, K. Kalantar-Zadeh, *Nanoscale Horiz.* **2022**, *7*, 141.
- [4] G. A. Breaux, B. Cao, M. F. Jarrold, *J. Phys. Chem. B* **2005**, *109*, 16575.
- [5] J. Tang, S. Lambie, N. Meftahi, A. J. Christofferson, J. Yang, M. B. Ghasemian, J. Han, F.-M. Alliou, M. A. Rahim, M. Mayyas, T. Daeneke, C. McConville, K. G. Steenbergen, R. B. Kaner, S. P. Russo, N. Gaston, K. Kalantar-Zadeh, *Nat. Nanotechnol.* **2021**, *16*, 431.
- [6] S. A. Idrus-Saidi, J. Tang, S. Lambie, J. Han, M. Mayyas, M. B. Ghasemian, F.-M. Alliou, S. Cai, P. Koshy, P. Mostaghimi, K. G. Steenbergen, A. S. Barnard, T. Daeneke, N. Gaston, K. Kalantar-Zadeh, *Science* **2022**, *378*, 1118.
- [7] C. Chiew, M. J. Morris, M. H. Malakooti, *Mater Adv* **2021**, *2*, 7799.
- [8] K. Kalantar-Zadeh, J. Tang, T. Daeneke, A. P. O'Mullane, L. A. Stewart, J. Liu, C. Majidi, R. S. Ruoff, P. S. Weiss, M. D. Dickey, *ACS Nano* **2019**, *13*, 7388.
- [9] M. Baharfar, J. Zheng, R. Abbasi, S. Lim, V. Kundi, P. V. Kumar, M. A. Rahim, C. Zhang, K. Kalantar-Zadeh, M. Mayyas, *Chem. Mater.* **2022**, *34*, 10761.
- [10] M. Mayyas, K. Khoshmanesh, P. Kumar, M. Mousavi, J. Tang, M. B. Ghasemian, J. Yang, Y. Wang, M. Baharfar, M. A. Rahim, W. Xie, F. M. Alliou, R. Daiyan, A. R. Jalili, D. Esrafilzadeh, K. K. Kalantar-zadeh, *Adv. Funct. Mater.* **2022**, *32*, 2108673.
- [11] W. P. Utomo, M. K. H. Leung, Z. Yin, H. Wu, Y. H. Ng, *Adv. Funct. Mater.* **2022**, *32*, 2106713.
- [12] H. Xu, Y. Ma, J. Chen, W. Zhang, J. Yang, *Chem. Soc. Rev.* **2022**, <https://doi.org/10.1039/D1CS00857A>.
- [13] B. H. R. Suryanto, H.-L. Du, D. Wang, J. Chen, A. N. Simonov, D. R. MacFarlane, *Nat. Catal.* **2019**, *2*, 290.
- [14] L. Zhai, S. Liu, Z. Xiang, *Ind. Chem. Mater.* **2023**, *1*, 332.

- [15] J. Hou, M. Yang, J. Zhang, *Nanoscale* **2020**, *12*, 6900.
- [16] B. Yang, W. Ding, H. Zhang, S. Zhang, *Energy Environ. Sci.* **2021**, *14*, 672.
- [17] D. Liu, M. Chen, X. Du, H. Ai, K. H. Lo, S. Wang, S. Chen, G. Xing, X. Wang, H. Pan, *Adv. Funct. Mater.* **2021**, *31*, 2008983.
- [18] Y. Zeng, C. Priest, G. Wang, G. Wu, *Small Methods* **2020**, *4*, 2000672.
- [19] J. Sun, T. Zhang, J. Hong, R. Zhou, H. Masood, R. Zhou, A. B. Murphy, K. K. Ostrikov, P. J. Cullen, E. C. Lovell, R. Amal, A. R. Jalili, *Chem. Eng. J.* **2023**, *3*, 143841.
- [20] J. Sun, D. Alam, R. Daiyan, H. Masood, T. Zhang, R. Zhou, P. J. Cullen, E. C. Lovell, A. R. Jalili, R. Amal, *Energy Environ. Sci.* **2021**, *14*, 865.
- [21] T. R. Das, S. Patra, R. Madhuri, P. K. Sharma, *J. Colloid Interface Sci.* **2018**, *509*, 82.
- [22] N. Han, Y. Wang, H. Yang, J. Deng, J. Wu, Y. Li, Y. Li, *Nat. Commun.* **2018**, *9*, 1320.
- [23] L. Li, C. Tang, B. Xia, H. Jin, Y. Zheng, S.-Z. Qiao, *ACS Catal.* **2019**, *9*, 2902.
- [24] F. Wang, R. Tang, H. Yu, P. C. Gibbons, W. E. Buhro, *Chem. Mater.* **2008**, *20*, 3656.
- [25] S. C. Warren, A. C. Jackson, Z. D. Cater-Cyker, F. J. DiSalvo, U. Wiesner, *J. Am. Chem. Soc.* **2007**, *129*, 10072.
- [26] J. Wu, F. Qin, Z. Lu, H.-J. Yang, R. Chen, *Nanoscale Res. Lett.* **2011**, *6*, 66.
- [27] X. Yu, A. Li, C. Zhao, K. Yang, X. Chen, W. Li, *ACS Nano* **2017**, *11*, 3990.
- [28] R. G. T. Rosa, C. de Araujo Duarte, W. H. Schreiner, N. P. M. Filho, A. G. Bezerra Jr, A. Barison, F. M. M. Ocampos, *Colloids Surf. A* **2014**, *457*, 368.
- [29] H. Safardoust-Hojaghan, M. Salavati-Niasari, M. H. Motaghefard, S. M. Hosseinpour-Mashkani, *New J. Chem.* **2015**, *39*, 4676.
- [30] C. Xing, W. Huang, Z. Xie, J. Zhao, D. Ma, T. Fan, W. Liang, Y. Ge, B. Dong, J. Li, H. Zhang, *ACS Photonics* **2018**, *5*, 621.
- [31] H. Okamoto, *J Phase Equilibria Diffus* **2015**, *36*, 292.
- [32] J. W. Christian, *Equilibrium and General Kinetic Theory*, 2nd ed., Pergamon Press, Oxford, **1975**.
- [33] S. Karthika, T. K. Radhakrishnan, P. Kalaichelvi, *Cryst. Growth Des.* **2016**, *16*, 6663.
- [34] V. M. Fokin, E. D. Zotto, *J Non Cryst Solids* **2000**, *265*, 105.
- [35] C. Rüssel, R. Keding, *J Non Cryst Solids* **2003**, *328*, 174.
- [36] D. A. Porter, K. E. Easterling, *Phase Transformations in Metals and Alloys (Revised Reprint)*, 3rd ed., CRC press, Boca Raton, FL **2009**.
- [37] M. J. Regan, P. S. Pershan, O. M. Magnussen, B. M. Ocko, M. Deutsch, L. E. Berman, *Phys. Rev. B* **1997**, *55*, 15874.
- [38] E. DiMasi, H. Tostmann, B. M. Ocko, P. S. Pershan, M. Deutsch, *J. Phys. Chem. B* **1999**, *103*, 9952.
- [39] O. Shpyrko, M. Fukuto, P. Pershan, B. Ocko, I. Kuzmenko, T. Gog, M. Deutsch, *Phys. Rev. B* **2004**, *69*, 245423.
- [40] S. Zhao, J. F. Li, L. Liu, Y. H. Zhou, *Mater. Charact.* **2009**, *60*, 519.
- [41] B. Chanda, G. Potnis, P. P. Jana, J. Das, *J. Alloys Compd.* **2020**, *827*, 154226.
- [42] R. Goetzinger, M. Barth, D. M. Herlach, *Acta Mater.* **1998**, *46*, 1647.
- [43] Q. J. Zhai, Y. L. Gao, W. B. Guan, K. D. Xu, *Mater. Sci. Eng., A* **2006**, *441*, 278.
- [44] A. Turchanin, W. Freyland, D. Nattland, *Phys. Chem. Chem. Phys.* **2002**, *4*, 647.
- [45] T. Gancarz, *J. Mol. Liq.* **2022**, *363*, 119912.
- [46] A. H. Ayyad, W. Freyland, *Surf. Sci.* **2002**, *506*, 1.
- [47] T. Xian, X. Sun, L. Di, Y. Zhou, J. Ma, H. Li, H. Yang, *Catalysts* **2019**, *9*, 1031.
- [48] X. Li, Y. Sun, T. Xiong, G. Jiang, Y. Zhang, Z. Wu, F. Dong, *J. Catal.* **2017**, *352*, 102.
- [49] J. Sun, R. Zhou, J. Hong, Y. Gao, Z. Qu, Z. Liu, D. Liu, T. Zhang, R. Zhou, K. K. Ostrikov, P. Cullen, E. C. Lovell, R. Amal, R. Jalili, *Appl. Catal. B* **2024**, *342*, 123426.
- [50] N. Comisso, S. Cattarin, S. Fiameni, R. Gerbasi, L. Mattarozzi, M. Musiani, L. Vázquez-Gómez, E. Verlato, *Electrochem. Commun.* **2012**, *25*, 91.
- [51] M. Yang, B. Li, S. Li, Q. Dong, Z. Huang, S. Zheng, Y. Fang, G. Zhou, X. Chen, X. Zhu, *Nano Lett.* **2023**, *23*, 7733.
- [52] W. Guo, C. Yu, S. Li, J. Qiu, *Energy Environ. Sci.* **2021**, *14*, 576.
- [53] G. Soloveichik, M. Acharya, H. Cheeseman, D. Wicks, D. Tew, *US DOE* **2016**, <https://arpa-e.energy.gov/technologies/programs/refuel>.
- [54] R. Jalili, S. H. Aboutalebi, D. Esrafilzadeh, K. Konstantinov, J. M. Razal, S. E. Moulton, G. G. Wallace, *Mater. Horiz.* **2014**, *1*, 87.
- [55] R. Jalili, S. H. Aboutalebi, D. Esrafilzadeh, K. Konstantinov, S. E. Moulton, J. M. Razal, G. G. Wallace, *ACS Nano* **2013**, *7*, 3981.
- [56] A. R. Jalili, A. Satalov, S. Nazari, B. H. R. Suryanto, J. Sun, M. B. Ghasemian, M. Mayyas, A. E. Kandjani, Y. M. Sabri, E. Mayes, S. K. Bhargava, J. Araki, C. Zakri, P. Poulin, D. Esrafilzadeh, R. Amal, *ACS Appl. Mater. Interfaces* **2021**, *13*, 28627.
- [57] X.-D. Liang, N. Tian, S.-N. Hu, Z.-Y. Zhou, S.-G. Sun, *Mater. Rep.: Energy* **2023**, *13*, 100191.
- [58] S. Choi, C. Kim, J. M. Suh, H. W. Jang, *Carbon Energy* **2019**, *1*, 85.
- [59] A. S. Lorenzetti, T. Sierra, C. E. Domini, A. G. Lista, A. G. Crevillen, A. Escarpa, *Sensors* **2019**, *20*, 76.
- [60] W. Song, L. Yue, X. Fan, Y. Luo, B. Ying, S. Sun, D. Zheng, Q. Liu, M. S. Hamdy, X. Sun, *Inorg. Chem. Front.* **2023**, <https://doi.org/10.1039/D3Q100554B>.